The final publication is available at

http://dx.doi.org/10.1364/OE.24.012093

Reconfigurable lattice mesh designs for programmable photonic processors

Daniel Pérez,[1] Ivana Gasulla,[1] José Capmany[1*] and Richard A. Soref[2]

[1]ITEAM Research Institute, Universitat Politècnica de València, Camino de Vera s/n, 46022 Valencia, Spain
[2]Department of Engineering, University of Massachusetts Boston, Boston, MA 02125, USA
[*]jcapmany@iteam.upv.es

Abstract: We propose and analyse two novel mesh design geometries for the implementation of tunable optical cores in programmable photonic processors. These geometries are the hexagonal and the triangular lattice. They are compared here to a previously proposed square mesh topology in terms of a series of figures of merit that account for metrics that are relevant to on-chip integration of the mesh. We find that that the hexagonal mesh is the most suitable option of the three considered for the implementation of the reconfigurable optical core in the programmable processor.

References and links

1. "Birth of the programmable optical chip," Nature Photon. **10**, 1 (2016).
2. J. Capmany and D. Novak, "Microwave photonics combines two worlds," Nat. Photonics **1**, 316-330 (2007).
3. J. Yao, "Microwave photonics," J. Lightwave Technol. **27**(3), 314-335 (2009).
4. J. E. Mitchell, "Integrated wireless backhaul over optical access networks," J. Lightwave Technol. **32**(20), 3373-3382 (2014).
5. M. K. Smit et al., "An introduction to InP-based generic integration technology," Semiconductor Science and Technology **29** (8), 083001 (2014)
6. D. Pérez, I. Gasulla, and J. Capmany, "Software-defined reconfigurable microwave photonics processor," Opt. Express **23**, 14640-14654 (2015).
7. J. Capmany, I. Gasulla, and D. Pérez, "Microwave photonics: The programmable processor," Nature Photon. **10**, 6-8 (2016).
8. L. Zhuang, C.G.H. Roeloffzen, M. Hoekman, K-J. Boller, and A.J. Lowery,. "Programmable photonic signal processor chip for radiofrequency applications," Optica **2**, 854-859 (2015).
9. W. Liu et al., "A fully reconfigurable photonic integrated signal processor," Nature Photon. **10**, 190-195 (2016).
10. R. A. Soref, "Mid-infrared 2 × 2 electro-optical switching by silicon and germanium three-waveguide and four-waveguide directional couplers using free-carrier injection," Photon. Res. **2**, 102-110 (2014)
11. C. G. Roeloffzen et al., "Silicon nitride microwave photonic circuits," Opt. Express **21**(19), 22937–22961 (2013).

1. Introduction

A recent editorial [1] has identified programmable general photonic processors as a key evolution path towards the implementation of a next generation of advanced photonic systems, which will be required in massive scale application scenarios such as 5G communications and the Internet of Things (IoT) [2-4]. Contrary to the paradigm of application specific photonic integrated chips (ASPICs), where a specific cicuit architecture is designed to implement a specific functionality, the general photonic processor vision brings the promise of implementing several functionalities by suitable programming of a common photonic hardware architecture. The realization of this vision will also bring additional advantages in terms of low cost and enhanced reliability fabrication when combined with Generic Integration (GIM) and Generic Foundry (GFM) Models [5]. Recent works have addressed the design of general photonic processors both for analog [6-8] and digital [9]

applications. The central element of the reconfigurable optical processor is the optical core, where the main signal processing tasks are carried in the photonic domain. Ideally, the optical core should be built upon a versatile architecture capable of implementing different functionalities in response to different electronic control signals. In practice, the main proposed configurations for this core are based on the cascade of finite (i.e. Mach-Zehnder interferometers) and infinite (i.e. Ring Cavity) impulse response cells. Recently however, Zhuang and co-workers [8] have proposed a design for a programmable optical core that is inspired by the photonic FPGA-like concept. This approach is based on a 2D waveguide square mesh network where the connections between waveguides are controlled by means of tunable Mach–Zehnder interferometers (MZIs). Through external electronic control signals, each MZI can be configured to operate as a directional coupler or simply as an optical switch in a cross or bar state providing amplitude- and phase-controlled optical routing. In this way, the combination of different MZIs in the 2D square grid, -each individually configured as desired-, enables the synthesis of any kind of optical core circuit topology, including finite and infinite impulse response filters.

Notwidthstanding, space and power consumtion contraints play a critical role in the design of photonic circuits in general and of optical meshes in particular. The limited area available for growing the optical mesh, and the need to reduce to a minimum the number of switching elements required to implement a set of optical core topologies call for a careful analysis of possible geometries for the mesh topology implementing the optical core. In this paper we propose and analyze two alternative designs: the triangular and the hexagonal mesh and compare them with the square design proposed in [8]. After providing in Section 2 the basic definitions of the relevant mesh elements and parameters, which are employed in the rest of the paper, we develop the pertinent analysis and comparison in Section 3. Geometries are compared in terms of several figures of merit, which account for footprint and number of switching elements per unit area, spectral period resolution, flexibility or reconfiguration capability, bending radii and losses. We find that the hexagonal geometry outperforms both the triangular and the square for most of the benchmarking parameters. In Section 4 we further detail the comparison between the mesh designs by considering a specific but representative application case. Finally, we summarize and conclude the paper in Section 5.

2. Novel reconfigurable mesh designs and basic definitions

We propose two new configurations of tunable coupler-based meshes that can synthetize photonic integrated circuit designs. Figures 1(a) and (b) illustrate the novel hexagonal and triangular meshes, respectively, and their associated interconnections schemes at the bottom. As in the square-type mesh, illustrated for comparison in Fig. 1(c) [8], the basic building block of these meshes is a tunable coupler that must provide, independently, a complete splitting ratio tuning and phase response. This switching/tapping/dephasing mechanism can be obtained either by exploiting the electro-refraction and/or the electro-absorption effect [10], or by means of the thermo-optic effect [11], in a broadband 3-dB balanced Mach-Zehnder Interferometer (MZI). By configuring each tunable coupler placed at each side of the cell as a switch (in either its cross or bar state) or as a tunable coupler, one can synthesize a given photonic integrated circuit topology, as shown in [8].

The upper part of Fig. 2 shows the tunable basic unit (TBU) composed by the tunable coupler and its access (input/output) waveguides, which are a function of the bending radii and vary for each mesh due to variation of the angle between elements. The basic unit length (BUL) is:

$$BUL = L_{access} + L_{Tunable-Coupler}, \tag{1}$$

where L_{access} is the overall length of the access waveguide segment and $L_{Tunable-Coupler}$ is the length of the tunable coupler.
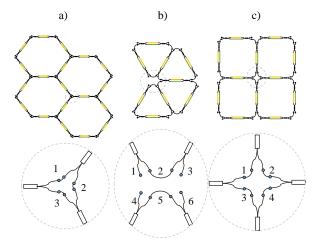
Fig. 1. Reconfigurable Mesh designs (upper): (a) Hexagonal type , (b) triangular type, (c) square type [8], and their associated interconnections points (bottom).

Although different structures of tunable couplers can be considered in principle (balanced and unbalanced 2x2 couplers, 3x3, and 3-dB MZIs), in this paper we will only consider 3-dB balanced Mach-Zehnder Interferometer (MZI) structures loaded with a heater on each arm, as illustrated in the lower part of Fig. 2. Nevertheless, the treatment is not restricted to this case.
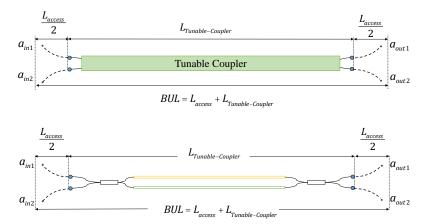

Fig. 2. (Upper) Labeled schematic of a general tunable coupler acting as the basic building block of the mesh. The Basic Unit Length (BUL) is illustrated as the sum of the tunable coupler length and the arc length of the access waveguides. (Lower) Particular case of a MZI-based tunable coupler.

Referring to the lower part of Fig. 2, the tunable basic unit can implement 3 different states: *cross state switch* (light path connects a_{in1} to a_{out2} and a_{in2} to a_{out1}), *bar state switch* (light path connects a_{in1} to a_{out1} and a_{in2} to a_{out2}) and *tunable splitter*.

For a balanced MZI loaded with heaters on both arms, the splitting ratio is obtained by increasing the effective index due to the Joule effect in one arm. Once set, a common drive in both heaters will provide a common phase shift, leading to independent control of the amplitude ratio and the phase. The device is characterized by its insertion losses (*IL*) and extinction ratio parameters (*ER_{Bar}* and *ER_{Cross}*):

$$IL(dB) = 10\log_{10}\left(\frac{|a_{out1}|^2 + |a_{out2}|^2}{|a_{in1}|^2 + |a_{in2}|^2}\right), \qquad ER_{Bar/Cross}(dB)\Big|_{\substack{|a_{in1}|^2=1 \\ |a_{in2}|^2=0}} = 10\log_{10}\left(\frac{|a_{out2/1}|^2}{|a_{out1/2}|^2}\right). \qquad (2)$$

These provide valuable information regarding the losses of the tunable units and since they are connected in cascade configuration to build up the mesh, the overall *IL* of the synthetized device will be the sum of the *IL* corresponding to the units across which the light has travelled. As an example, if we assume overall device losses of 10 dB and *IL* of 0.2 dB for each TBU, then the longer path will be limited to 50 units.

We consider a design whereby the unit is in cross state in absence of applied bias. In order to reduce the footprint of the synthetized circuits, we allow the possibility of using all the unit ports independently. For example, in a cross state set both *in*1/*out*2 and *in*2/*out*1 connections can be employed.

3. Analysis and comparison among the three mesh designs

We now analyze and compare the performance of the hexagonal, triangular and square mesh designs in terms of a set of figures of merit, which are relevant from a chip integration point of view. For each case, the figure of merit is defined and the quality criterion specified. Finally, we consider the overall perfomance of each mesh design taking into consideration all the defined figures of merit.

3.1 Spatial tuning resolution step and reconfiguration performance

Meshes will be usually employed and reconfigured to implement either finite impulse response (Mach Zehnder Interferometers, MZI) or infinite impulse response (Optical Ring Resonator, ORR) filters. These filters are spectrally periodic and the Free Spectral Range (FSR) is inversely proportional to the length mismatch between the two arms in the case of MZIs or the cavity length in the case of ORRs. The spatial tuning resolution step quantifies which is the minimum step in BUL units by which the arm length mismatch or the cavity length can be increased/decreased. The smaller the value of this figure of merit, the better, as this allows a finer discrete spatial sampling and therefore a wider range of cavity lengths (L_{ORR} in the case of ORRs) or arm length mistmatch values (ΔL_{MZI} in the case of MZIs). The latter will determine $\Delta \nu_{FSR}$, the frequency separation corresponding to the spectral period FSR of the filter:

$$\Delta \nu_{FSR} = \frac{c}{n_g X}, \tag{3}$$

where n_g is the group index of the waveguide and $X=L_{ORR}$ or $X=\Delta L_{MZI}$ depending on whether an ORR or a MZI is considered. Notice as well that more complex configurations, like coupled resonator optical waveguides (CROWs), side-coupled integrated spaced sequence of resonators (SCISSORs) and ring-loaded MZIs, can be configured with any mesh, but in principle, these will be built upon combination of the basic ORR and MZI structures.

For a fixed BUL, each mesh design has a different spatial resolution capacity for synthezising the length of the cavities and the arm length differences of the interferometric structures. For instance, Figs. 3 and 4 illustrate an example of particular implementations of ORRs and MZIs with hexagonal and triangular mesh designs, respectively. Notice that this particular hexagonal MZI configuration re-uses one tunable coupler inside one of the arms that is set in cross state.
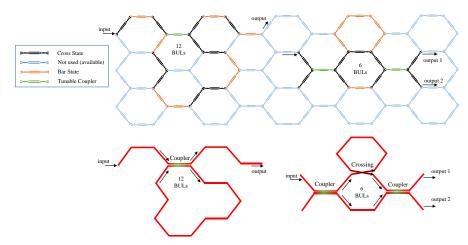
Fig. 3. Optical Ring Resonator (left) and Mach-Zehnder Interferometer (right) configurations over an hexagonal mesh (up) and corresponding light paths (bottom).
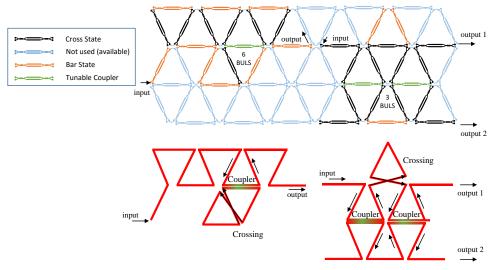

Fig. 4. Optical Ring Resonator (left) and Mach-Zehnder Interferometer (right) configurations over a triangular mesh (up) and corresponding light paths (bottom).

The results of our comparative analysis are shown in Table 1.

Table 1. Values for the possible cavity lengths (ORR) and arm length mismatch (MZI) in BUL units for the different mesh designs, $n \in N$ {0,1,2,…} for MZIs and $n \in N$ {1,2,3,…} for ORRs

	Square	Triangular	Hexagonal
MZI	$\Delta L_{MZI}^{Sq} = 4n$	$\Delta L_{MZI}^{Tr} = 3n$	$\Delta L_{MZI}^{Hx} = 2n$
ORR	$L_{ORR}^{Sq} = 4n$	$L_{ORR}^{Tr} = 3n$	$L_{ORR}^{Hx} = \{6, 10 + 2n\}$

Regarding ORR configurations, the triangular mesh offers the maximum achievable FSR. For cavity lengths above 10 BULs, the hexagonal mesh doubles the resolution of the square mesh. As far as MZIs configurations are concerned, the hexagonal mesh offers the maximum achievable FSR and, again, doubles the resolution of the square mesh. Both new proposed meshes improve the spatial tuning resolution of the square mesh. The results show that, in

general, the finest spatial tuning resolution corresponds to the hexagonal mesh with a step of 2 BULs, although the smallest cavity value in the case of implementing an ORR is 6 BULs followed by a second step in 4 BUL units. Given a maximum value available for X, we define the reconfiguration performance of the mesh as the number of filters with different $\Delta\nu_{FSR}$ values that can be implemented. Figure 5 plots this figure of merit for the square, triangular and hexagonal meshes as a function of X for the ORR (upper) and MZI (lower) filters.
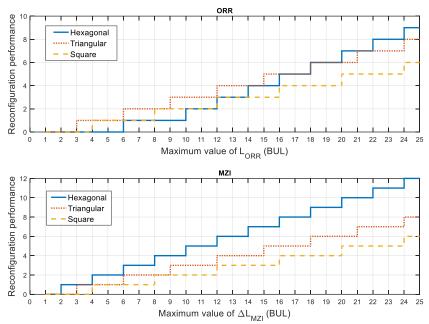

Fig. 5. Reconfiguration performance vs available maximum value of X expressed as an integer number n of the *BUL* for the square, triangular and hexagonal meshes. ORR (upper) and MZI (lower) designs.

Note that the hexagonal configuration clearly features the best reconfiguration performance as compared to the triangular and the square meshes for MZI implementation. In the case of ORRs, the hexagonal and triangular meshes provide similar results.

3.2 Number of switching elements per unit area

From a standalone point of view of integration density, a mesh having a number of switching elements as high as possible should be preferrable. However, in practice, additional factors lead to a different conclusion when taken into consideration. First of all, the maximum number of TBUs that build up the longest light path will be limited by its non-ideal propagation and coupling characteristics. In addition, if the tuning mechanism requires metal layers to route the control signals that take up the same layer level, a reduced figure of switching elements per area facilitates this task offering a reduction in the BUL since there is no need to increase the length of the access waveguides to provide a free way to the metal tracks. If the wirebonding alternative is preferred, it is also desirable since there is more free space available to prevent the crossing of wires by increasing the separation between metal junctions. Also, in the case of using a MZI as the tunable basic unit, a reduced value of this figure of merit offers extra free space to grow further apart the arms of each MZI, reducing the crosstalk due to the tuning mechanism, i.e., thermal crosstalk in this case. Finally, a higher number of switching elements per unit area leads to more power hungry configurations and does not necessarily mean more flexibility in reconfiguration performance. Thus, for equal reconfiguration performance, a mesh design having a number of switching elements per unit area as low as possible is preferred.

The footprint of the mesh is obtained first by computing the area of the unitary cell and then by multiplying by the number of cells. For the sake of comparison, we normalize the polygons that define each unit cell (square, hexagon and triangle) by their side, i.e., all the meshes have sides with the same BUL. In this way, we neglect the waveguide access difference between meshes, which is the case when the BUL is large as compared to the bending radii of the technology of integration. The unit cell area can be expressed in general as $A_{unit\text{-}cell} = kBUL^2$, where $k = 1$ for the square cell, $k = 3\sqrt{3}/2$ for the hexagonal cell and $k = \sqrt{3}/4$ for the triangular cell. For reference, as it will be shown in Section 4, if we consider a square normalized area of 25 BUL^2, it is straightforward to obtain that the number of switching elements per normalized area is 2.4 for the square mesh, 1.52 for the hexagonal mesh and 3.96 for the triangular mesh.

3.3 Replication flexibility: Number of possible alternative geometries for filter implementation

Another important figure of merit is the mesh replication flexibility defined as the number of possible different alternative geometries that a given mesh design provides to implement a given ORR (with a fixed cavity length) or MZI configuration (with a fixed arm length imbalance). This metric is a good indicator of the potential for configuring complex devices.

When a new photonic device needs to be added in an already operational mesh, it will occupy the available free space. The more flexible the mesh architecture, the easier it will be to allocate it within the spare space. To make a fair comparison between the proposed designs, we have considered the synthesis in an infinity mesh of ORRs with cavity lengths of up to 16 BULs and MZIs with arm imbalances of up to 12 BULs. Since the MZIs' FSR depend on the difference between the arm lengths, we have limited the analysis to the shorter paths designs. The results of our analysis are shown in Table 2. The two final rows in the table provides a cumulative figure on the total number of replication options and the replication ratio (compared to that of the triangular mesh) for the two scenarios (ORR and MZI) from which we can observe that the square mesh features a replication flexibility which is approximately double to that of the hexagonal mesh and this features approximately a 30% extra replication flexibility as that of the triangular mesh.

Table 2. Number of different devices that can be configured for each mesh design

	ORRs				MZIs		
L_{ORR} (BULs)	Square	Hexagonal	Triangular	ΔL_{MZI} (BULs)	Square	Hexagonal	Triangular
3	-	-	1	0	1	1	1
4	1	-	-	1	-	-	-
5	-	-	-	2	-	1	-
6	-	1	2	3	-	-	1
7	-	-	-	4	3	1	-
8	5	-	-	5	-	-	-
9	-	-	6	6	-	1	7
10	-	3	-	7	-	-	-
11	-	-	-	8	11	3	-
12	20	5	8	9	-	-	3
13	-	-	-	10	-	8	-
14	-	11	-	11	-	-	-
15	-	-	15	12	42	10	8
16	60	22	-	-	-	-	-
Total	86	42	32		57	25	19
Replication ratio	2.68	1.31	1		3	1.31	1

Figure 6 illustrates, as a representative example, the case of setting ORRs of the same length in bus configuration (SCISSORs). The upper left part shows, for instance, the unique 3 ways of synthetizing ORRs of normalized circumference length equal to 10 BULs using an hexagonal mesh. For the triangular mesh, the two alternatives of synthetizing ORRs of normalized circumference length equal to 6 BULs are shown in the upper right part of Fig. 6. Finally, the lower part of Fig. 6 shows the unique five alternatives to ORRs of normalized length 8 BUL using a square mesh. Notice that the first 3 designs need also the re-use of one of the TBUs. It is also worth mentioning that different devices could also share TBUs in order to save space. For example, in the square mesh, between the ORR8A and the ORR8B an ORR8R1C could be synthetized sharing their outer bar-state-configured TBUs. Here the nomenclature employed is the following: DEVNRML where DEV={ORR,MZI} stands for the device implemented, N is the cavity or arm length mismatch in BUL units, R appears if coupler reutilization is employed, M is the number of re-utilized couplers and L={A,B,C,...} is a letter that designates different designs sharing equal values for the preceeding parameters in the code.
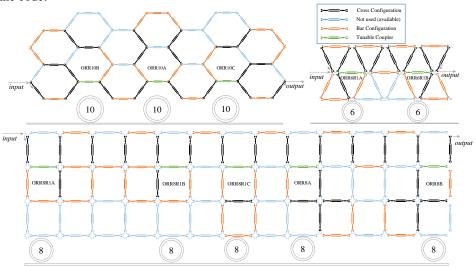

Fig. 6. Different mesh types configurated to synthezise cascaded ORRs in different geometries.

The results from Table 2 confirm that the square mesh is the most flexible when replicating the same device but, at the same time, they outline that this mesh design is the most restrictive one in terms of spatial tuning resolution step. On the other hand, the triangular mesh is the most restrictive in terms of replication flexibility due to its mesh complexity and its interconnection scheme, as it is shown at the bottom of Fig. 1. Nevertheless, its spatial tuning resolution step is better than the square mesh. Finally, the hexagonal mesh presents a good equilibrium between medium flexibility and the highest spatial tuning resolution step.

3.4 Losses and spatial resolution associated with TBU interconnections

Interconnections between the TBUs determine the spatial resolution and the losses due to bending radii and polarization rotation. To make a fair comparison between the meshes, we consider two benchmarking alternatives. In both cases the tunable coupler length of the TBU is kept constant: In the first one the bending radii of the curves are fixed while in the second it is the BUL that is kept constant.

In the first case, the fixed radius is dictated by the integration technology platform. It ranges typically from 5-30 µm in silicon waveguides to 100-250 µm in Indium Phosphide, 100-1000 µm for Silicon Nitride platforms and about 1000 µm for Silica on Silicon. In this case, the BUL of each mesh will be different as it depends on a fixed term (the tunable coupler length) and a variable term (the access length) defined by:

$$L_{access(both)} = \frac{2\pi Ra}{(360/\alpha)}, \tag{4}$$

where α is the angle in degrees of the arc defined by the interconnection, and Ra the radius of curvature. Both of them are illustrated in Fig. 7 for each mesh design. Since the angle required by the square, hexagonal and triangular meshes are 90º, 60º and 120º, respectively, then the access length the hexagonal mesh is a 33.00% shorter compared to the square mesh while it is a 33.00% longer for the triangular mesh compared to the square mesh.
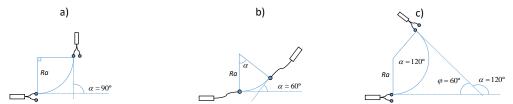

Fig. 7. Access length and angle definition for each mesh: (a) square, (b) hexagonal, (c) triangular.

Therefore, when the radius of curvature is fixed, the BUL and, thus the spatial resolution, will be different for each mesh. Figure 8 shows the relation between the BUL of a given mesh design to that of the square mesh as a function of the ratio between the access waveguides and the tunable coupler length. The range of applicability of this curve depends on the material platform used to implement the mesh. For instance, in silicon photonics, the bending radii of 5-30 µm, compared with a tunable coupler length of about 500 µm, places the region of application in the left side of the graph. In this case, the increase or decrease in the BUL associated to the triangular or the hexagonal meshes will be practically negligible as compared to that of the square mesh. In other platforms featuring higher values for the minimum bending radius, the region of application in Fig. 8 will move towards the right part of the graph, leading to a superior resolution for the hexagonal mesh.
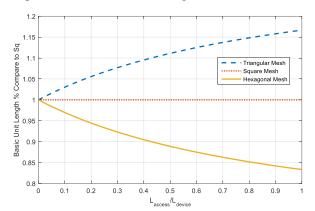

Fig. 8. Relation between the BUL of a given mesh design to that of the square mesh as a function of the ratio between the access waveguides and the tunable coupler length.

The second case for comparison consists in fixing the value of the BUL so the product $\alpha \cdot Ra$ shown in the right part of Eq. 4 remains fixed. In this case, the bending radius will be different for each mesh and, more precisely, when compared to the square mesh, the triangular will be a 25.00% smaller whereas the hexagonal will be a 50.00% higher. Here, since the losses associated to the bending radius and the polarization rotation are greater for shorter bending radii, the hexagonal features, again, the best performance.

3.5 Discussion

Table 3 summarizes the results of the previous subsections carried for the different figures of merit and the three mesh designs. With the exception of the replication ratio, the hexagonal mesh design is the most versatile option featuring the best results in all the figures of merit. Its superior performance in terms of spatial tuning resolution step allows for a higher reconfiguration performance, that is, a wider range of spectral periods that can be implemented with complex structures built upon combining ORR and MZI based filters. The reduced value in the number of switching elements per unit area allows simpler configurations in terms of fabrication, electrode deposition, control pad interconnections and power consumption. Finally, and equally important, the hexagonal lattice mesh provides shorter curved sections for a given access waveguide bending radius and a fixed BUL value, which, in turn, results in lower propagation losses.

We conclude therefore that the hexagonal mesh is, in general, the most suitable option of the three considered in this paper for the implementation of the reconfigurable optical core in the programmable processor.

Table 3. Summary of values for the figures of merit of the different mesh designs

Figure of Merit	Triangular	Square	Hexagonal
ORR cavity spatial tuning resolution step in BUL units (the lower the better)	3	4	2* The first step has a resolution of 6
MZI arm imbalance spatial tuning resolution step in BUL units (the lower the better)	3	4	2
ORR reconfiguration performance (the higher the better) (for X=25 *BUL*)	8	6	9
MZI reconfiguration performance (for X=25 *BUL*)	8	6	12
Switching elements per unit area (the lower the better for a fixed value of reconfiguration performance)	3.96	2.40	1.52
Replication Ratio for ORR structures up to 16 BUL cavity length (the higher the better).	1	2.68	1.31
Replication Ratio for MZI structures up to 12 BUL cavity length (the higher the better).	1	3	1.31
$L_{access}/L_{access\ square}$ % for a fixed Ra (the lower the better)	+33.33%	+0.00%	-33.33%
Ra/Ra_{square} % for a fixed BUL (the higher the better)	-25.00%	+0.00%	+50.00%

4. Comparative analysis for a specific application case

Once we have analyzed the three mesh designs, we provide a more detailed comparative study for a specific, but representative case. Here we consider a 5x5 BUL^2 available surface to implement the mesh and assume a silicon photonics platform featuring optical waveguide propagation losses of 2.5 dB/cm and a group index of $n_g = 4.2933$ at a wavelength of $\lambda = 1550$ nm. The TBUs are implemented by means of balanced 3-dB MZIs loaded in both arms with thermal tuners to provide independent amplitude ratio and phase tunability. The MMI couplers placed at the input/output of the MZI have excess losses of 0.1 dB each. The BUL is set to 700 μm, which allows a phase tuning beyond 2π preventing the burning of the tuning heater. With this value, the chip area is 12.25 mm^2, which is within the currrent range of

fabrication. The area can allocate, assuming negligible the impact of the access waveguide, 25 square, 9 hexagon or 57 triangle unit cells, and the number of switching elements (tunable couplers) will be 60 for the square mesh, 38 for the hexagonal and 99 for the triangular. Taking then into consideration the area of the unit cells given in section 3.2, it is straightforward to obtain that the number of switching elements per normalized area is 2.4 for the square mesh, 1.52 for the hexagonal mesh and 3.96 for the triangular mesh. In order to compensate the greater angle of the triangular mesh access waveguides and to provide a more squared layout, we have limited the triangular mesh to 54 cells. The longest path in the mesh is in the range of 22-24 *BULs* and therefore the number of structures with different FSR values can be anticipated from Fig. 5.

Figure 9 shows all the possible arrangements for ORRs up to 20 BULs in each of the three mesh designs (8 for the hexagonal, 7 for the triangular and 5 for the square), which match the results predicted by Fig. 5.
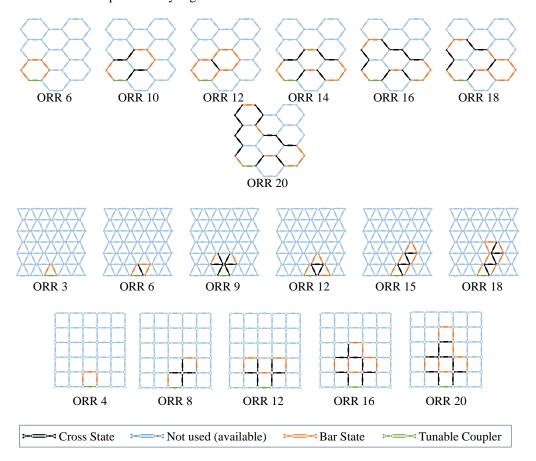

ORR 6   ORR 10   ORR 12   ORR 14   ORR 16   ORR 18

ORR 20

ORR 3   ORR 6   ORR 9   ORR 12   ORR 15   ORR 18

ORR 4   ORR 8   ORR 12   ORR 16   ORR 20

⊶⬯⊷ Cross State   ⊶⬯⊷ Not used (available)   ⊶⬯⊷ Bar State   ⊶⬯⊷ Tunable Coupler

Fig. 9. Optical Ring Resonator filters with different cavity lengths that can be implemented in a 5x5 BUL^2 area using the hexagonal, triangular and square mesh designs. ORR *Z* means an optical ring resonator filter with cavity length of *Z* BULs.

As we can check, the hexagonal mesh provides the highest number of different cavity lengths and thus of FSR values. Note, however, that the highest FSR value corresponds to the triangular mesh. Figure 10 depicts the spectral characteristics attainable with each mesh design where propagation and coupler losses have been taken into account. In each case, the coupling constant of the cavity coupler is adjusted to the critical couling ratio set by the cavity losses. Each spectrum can be finely tuned if necessary over a whole FSR period by empoying

one of the TBUs inside the cavity as a phase shifter. For reference, since one BUL corresponds to a FSR of 100 GHz, a cavity with length *kBUL* will render a filter with a FSR of 100/*k* GHz.
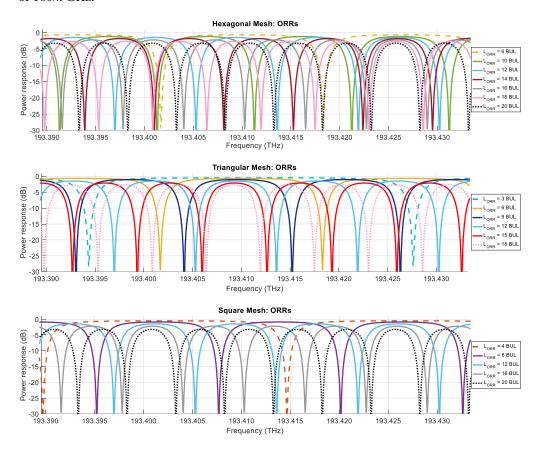

Fig. 10. Spectra of the different ORRs available for each mesh design option. In all the cases the cavity coupler is adjusted to attain critical coupling. Larger and shorter FSR are highlighted with dashed- and dotted-lines, respectively, for each mesh.

Figure 11 shows all the possible arrangements for MZIs up to 20 BULs in each of the three mesh designs (11 for the hexagonal, 7 for the triangular and 6 for the square), which match the results predicted by Fig. 5. Again, we can check that the hexagonal mesh provides the highest number of different cavity lengths and thus of FSR values. In this case there is a remarkable difference in the number of available FSR values as compared to the triangular and square meshes. The highest FSR value corresponds also to the hexagonal mesh.

The spectral characteristics attainable with each mesh design are shown in Fig. 12 where, as in the ORR case, propagation and coupler losses have been taken into account. Each spectrum can be finely tuned if necessary over a whole FSR period by employing one of the TBUs in one of the two arms of the MZI structure as a phase shifter. For reference since one BUL corresponds to a FSR of 100 GHz a path length mismatch of *kBUL* will render a filter with a FSR of 100/*k* GHz.
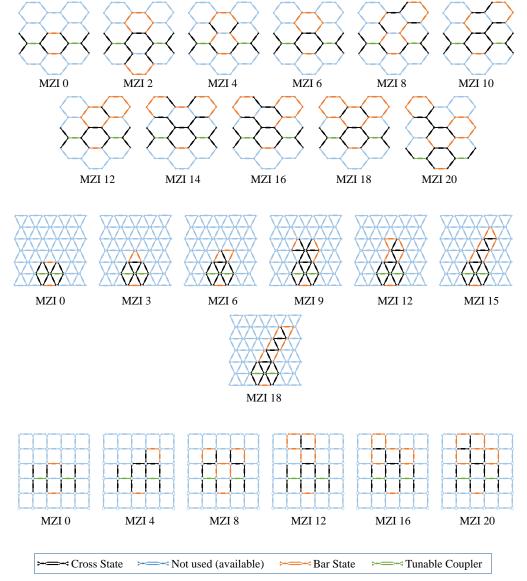
Fig. 11. Mach-Zehnder Interferometer Resonator filters with different path length mismatch that can be implemented in a 5x5 BUL² area using the hexagonal, triangular and square mesh designs. MZI *Z* means a Mach-Zehnder Interferometer filter with path length mismatch of *Z* BULs.

5. Summary and conclusions

We have proposed and analysed two novel mesh design geometries for the implementation of tunable optical cores in programmable photonic processors. These geometries are the hexagonal and the triangular lattices. They have been analyzed and compared to a previously proposed square mesh topology in terms of a series of figures of merit that have been defined in the paper to account for metrics relevant to on-chip integration of the mesh.

We have found that the hexagonal mesh configuration provides the best performance for most of the relevant metrics. These results can be relevant for the implementation of the reconfigurable optical core in the programmable processor.
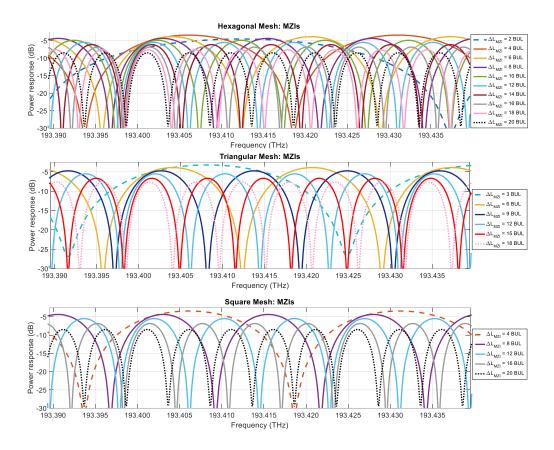
Fig. 12. Spectra of the different MZIs available for each mesh design option. In all the cases the output coupler is 50:50 and the input coupler is adjusted to attain maximal rejection (loss balancing).

Note that for both device configurations the larger the path is the higher the IL. This effect produced by the non-ideal characteristics of the TBUs, such as coupling and propagation losses, limits the maximum number of TBUs and, therefore, the size of the circuit.

Acknowledgments